α-Fe_2O_3 Nanotubes-Reduced Graphene Oxide Composites as Synergistic Electrochemical Capacitor Materials

Electronic Supplementary Information

Contents List

1.	Table S1 Electrochemical properties of various metal oxide-graphene materials composite electrodes explored in aqueous electrolytes	2
2.	Experimental section	3-5
3.	Fig. S1 UV-Vis absorption spectra of GO and rGO	6
4.	X-ray Photoelectron Spectroscopy Analysis Fig. S2 and S3 X-ray photoemission spectra (XPS) of Fe2p and C1s core levels. Table S2 Percentage of various oxygenated functional groups from deconvolution of the C1s peak	7-8
5.	Fig. S4 Ragone plot (power density vs. energy density) of α-Fe_2O_3 NTs and α-Fe_2O_3 NTs-rGO composites.	9
6.	Supplementary discussion on electrochemical capacitance performance of various iron oxides and iron oxide based composite materials in aqueous electrolyte in comparison with present study .	10-11
7.	Table S3 Electrochemical capacitance performance of various iron oxides and iron oxide based composite materials in aqueous electrolyte.	12
8.	References	13-14

Table S1. Electrochemical properties of various metal oxide-graphene materials composite electrodes explored in aqueous electrolytes

Pseudocapactive material	Graphene materials	Electrolyte	V. vs. Ag/AgCl	C_m (F/g)	Method	Ref.
MnO_2 microparticles	EG	1 M Na_2SO_4	-0.08 to 0.92	124	GS 0.1 A/g	2,3
MnO_2 nanorods	EG	2 M $(NH_4)_2SO_4$	-0.08 to 0.92	158	GS 2 mA/cm^2	4
ZnO nanoparticles	rGO	1 M KCl	-0.58-0.42	11.3	CV 10 mV/s	5
SnO_2 nanoparticles	rGO	1 M H_2SO_4	0 to 1	43.4	CV 2 mV/s	6
MnO_2 nanoneedles	GO	1 M Na_2SO_4	-0.08 to 0.92	216	GS 0.15 A/g	7
$Ni(OH)_2$ nanoplates	GS	1 M KOH	0 to 0.55	935	GS 2.8 A/g	8
Mn_3O_4 nanoparticles	rGO	1 M Na_2SO_4 6 M KOH	-0.28 to 0.72 -0.58 to 0.42	175 256	CV 5 mV/s	9
MnO_2 nanoparticles	rGO	1 M Na_2SO_4	-0.18 to 0.82	310	CV 2 mV/s	10
Co_3O_4 nanoparticles	rGO	6 M KOH	-0.08 to 0.32	243.2	CV 10 mV/s	11
$Co(OH)_2$ nanoparticles	rGO	6 M KOH	-0.28 to 0.42	972.5	GS 0.5 A/g	12
Fe_3O_4 nanoparticles	rGO	1 M KOH	-0.88 to 0.12	480	GS 5 A/g	13
ZnO nanoparticles	rGO	0.1 M Na_2SO_4	-0.08 to 0.92	308	GS 1 A/g	14
$[Co_{0.66}Al_{0.34}(OH)_2]^+$-nanosheets	GO	1 M KOH	0 to 0.55	1031	GS 1 A/g	15
α-$Ni(OH)_2$ nanoparticles	rGO	6 M KOH	0 to 0.45	1215	CV 5 mV/s	16
CeO_2 nanoparticles	rGO	6 M KOH	-0.08 to 0.42	208	GS 1 A/g	17

EG: exfoliated graphite; GO: graphene oxides; rGO: reduced graphene oxides; GS: graphene sheets

Experimental Section

Synthesis of rGO, α-Fe_2O_3 nanotubes (NTs), and α-Fe_2O_3 NTs-rGO composites

GO used in this work was prepared by the Hummers method. α-Fe_2O_3 NTs were synthesized by a hydrothermal treatment of $FeCl_3$ solution in the presence of $NH_4H_2PO_4$ at 220°C. Detailed procedures have been reported [1]. For the synthesis of α-Fe_2O_3 NTs-rGO composites, ~20 mg of GO was added to 0.4 mmol of α-Fe_2O_3 NTs and dispersed in 40 mL of deionized water. The dispersion was then hydrothermally treated at 180 °C for 24 h.

Characterizations

The morphologies of the as-synthesized nanocomposites were examined with a JEOL JSM-6400F field emission scanning electron microscope (FESEM) operating at 5 kV in high vacuum. TEM and HRTEM analysis, selected-area electron diffraction (SAED), and energy dispersive X-ray spectroscopy (EDS) were performed with a field-emission transmission electron microscope (TEM, JEOL, JEM 2010, accelerating voltage 200 kV). The crystal structure of the materials were analyzed by a Bruker D/MAX 2500 X-ray diffractometer with Cu K_α radiation λ = 1.54056 Å. Raman spectrum was recorded by a micro-Raman system (Jobin-Yvon T64000) with a typical laser power of 0.2 mW under ambient conditions. Elemental analyses were carried out on a Perkin-Elmer 2400 elemental analyzer. Based on elemental analyses, the weight percentage of rGO content is 16 wt % in the α-Fe_2O_3 NTs-rGO composite.

Preparation of working electrodes

The electrodes for the electrochemical studies were prepared by the doctor-blade technique using a mixture of the active materials (Fe_2O_3 NTs; rGO; Fe_2O_3 NTs-rGO), Super P carbon (MMM Ensaco) and binder (Kynar 2801) in the mass ratio 70:15:15, using N-Methylpyrrolidone (NMP) as the solvent for the binder. The slurry was pressed on an etched-copper foil (thickness, 15 μm, Alpha Industries Co Ltd., Japan) as current collector. The electrode area and mass of active material were 2 cm^2 and 3–4 mg. A Shimadzu Libror AEM 5200 electronic microbalance was used for weighing of the electrodes.

Electrochemical studies

An electrochemical half-cell was assembled in a three-electrode configuration with Pt wire as the counter electrode, Ag/AgCl (3 M KCl) as the reference electrode, and the above-mentioned prepared materials as working electrodes. In the setup of working electrode, the conductive side of the copper foil was placed on a gold plate connected to a Teflon-sealed copper rod. The front side of the copper foil (with active materials) was sealed with a Teflon cell with an O-ring. Thus the working electrode had a geometric area exposed to electrolyte of 0.785 cm^2 and contained about 1.2-1.5 mg of the above mentioned mixed slurry. All electrochemical measurements were carried out in 1 M Na_2SO_4 solution as electrolyte. Cyclic voltammetry (CV), galvanostatic charge-discharge (GS) studies, and electrochemical impedance spectroscopy (EIS) were conducted using an Autolab PGSTAT 30 potentiostat/ galvanostat at room temperature (~24 °C).

The specific capacitances C_m were calculated from the CV curved based on the following equation:

$$C_m = \frac{1}{mR\Delta V}\int I(V)dV$$

where m is the mass of active material, R is the scan rate, ΔV is the potential window of scanning, and the integral area under the CV curve.

The specific capacitances C_m were also calculated from the galvanostatic discharge curves using the equation as follows:

$$C_m = \frac{I}{\frac{\Delta V}{\Delta t}.m}$$

where $\Delta V/\Delta t$ is the average slope of the discharge curve after the IR drop, Δt is the discharge time, m is the active mass and I is the discharge current.

The energy density and power density can be further evaluated from the GS results using the following equations:

$$E = \frac{1}{2} C_m (\Delta V)^2$$

$$P = \frac{E}{t}$$

where E is the energy density and C_m is the specific capacitance, ΔV is the potential window, P is power density and t is the discharging time.

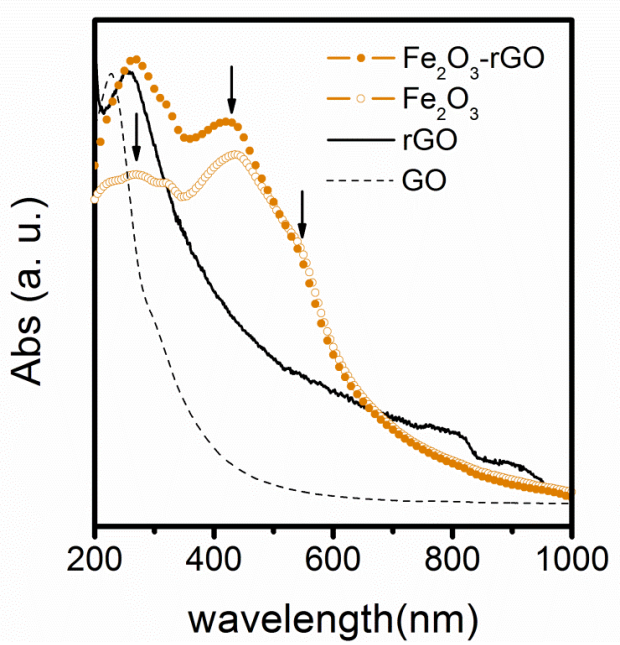

Fig. S1. UV-Vis absorption spectra of GO and rGO

The UV-vis absorption spectra show that the absorption peak (227 nm) of GO corresponding to $\pi \rightarrow \pi^*$ transitions of aromatic C=C bonds red-shifts to 257 nm after hydrothermal treatment at 180°C for 24 h. Together with the increase in absorption in the whole spectral region, these show that the hydrothermal treatment restores the electronic conjugation within the G nanosheets is restored. The small red shift of the Plasmon excitation peak of rGO from 257 to 266 nm in the α-Fe_2O_3 NTs composite indicates interaction between the π -electrons in r-GO and the α-Fe_2O_3 NTs in the resultant composite. The band at 427-437 nm is attributed to ligand to metal charge-transfer transitions of α-Fe_2O_3.

X-ray Photoelectron Spectroscopy Analysis

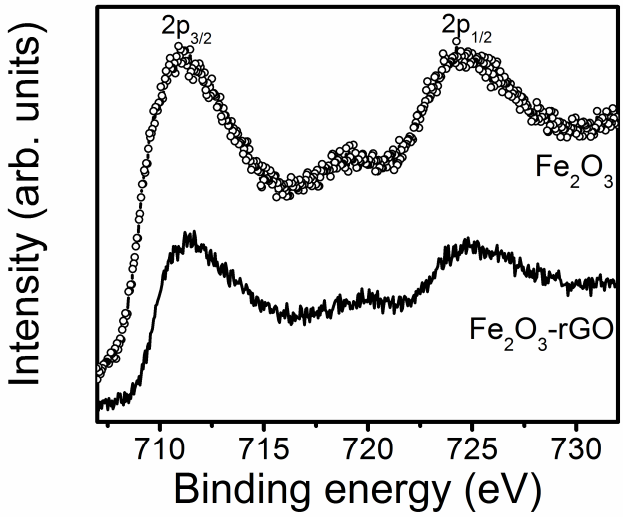

Fig. S1 High resolution Fe 2p core-level XPS spectra of the α-Fe_2O_3 and α-Fe_2O_3 -rGO.

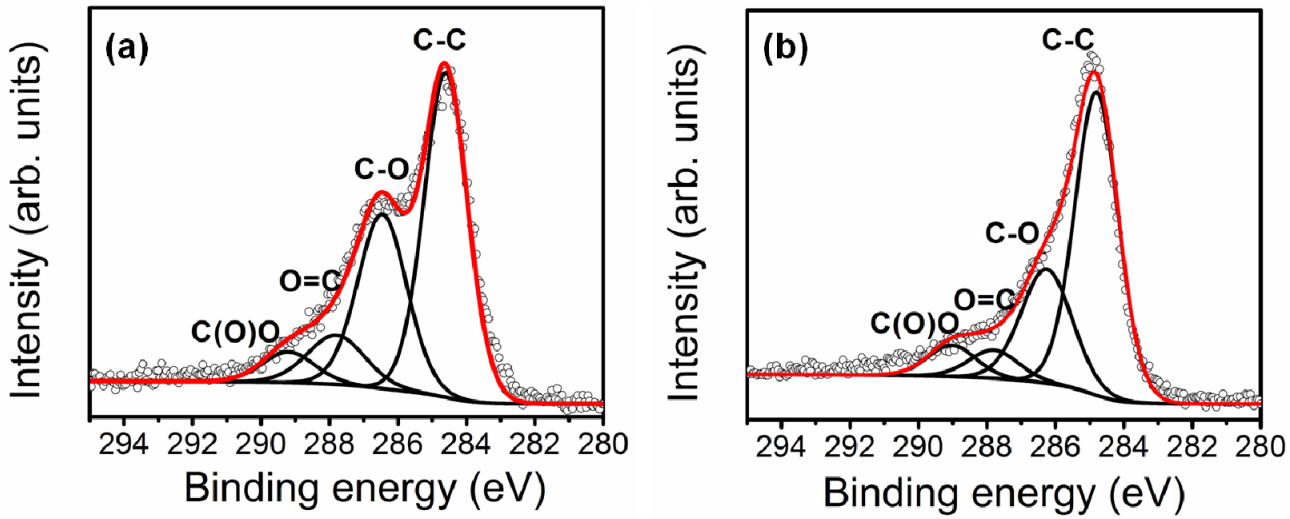

Fig. S3 High resolution C 1s core-level XPS spectra of (a) GO and (b) α-Fe_2O_3 –rGO.

Table S2. Percentage of various oxygenated functional groups

	C-C	C-O (epoxy)	C=O	C(O)O
B. E. (eV)	284.8	286.3	287.8	289.0
GO	52.1%	31.5%	9.4%	6.9%
Fe_2O_3-rGO	60.3%	26.5%	6.4%	6.9%

The Fe 2p spectral line shapes for the α-Fe_2O_3 and α-Fe_2O_3 –rGO are equivalent. The two major components at binding energies of 711.6 and 724.8 eV accompanied by a satellite are attributed to $2p_{3/2}$

and $2p_{1/2}$ core levels for α-Fe_2O_3. Figure S3 shows high-resolution narrow scans from the carbon region of GO and α-Fe_2O_3 –rGO, with the four most prominent deconvoluted components of the C 1s envelope shown in each panel, as summarized in Table S2. The original GO signal shows two separated peaks, as expected, due to the high percentage of oxygen functionalities. After the hydrothermal treatment, tailing at the higher binding energy region is reduced, which suggests that the decrease in relative content of carbon species bound to oxygen.

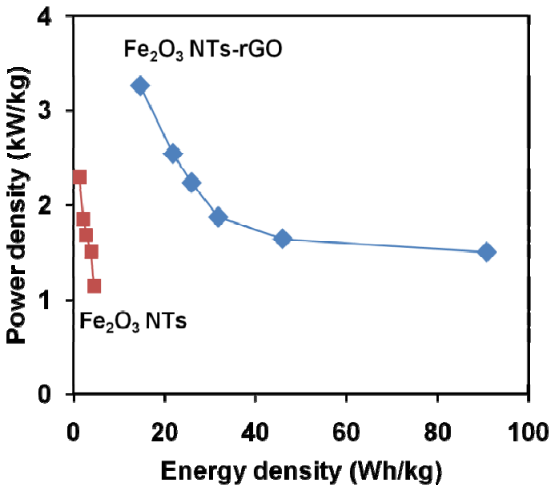

Fig. S4. Ragone plot (power density vs. energy density) of α-Fe_2O_3 NTs and α-Fe_2O_3 NTs-rGO composites. The energy and power densities were derived from GS data at various current densities.

Energy density and power density are two essential key factors for evaluating the power applications of ECs. In principle, calculation of energy and power density should base on electrochemical performance from full cells for practical means. This study focuses on development of negative electrode for asymmetric ECs and electrochemical data were obtained from half cells. Energy density and power density of α-Fe_2O_3 NTs and α-Fe_2O_3 NTs-rGO composites are calculated mainly for comparison and by no means to provide practical values. It must be noted that calculation of energy and power density based on capacitances measured from half cells often leads to overestimation of energy and power output (e.g. overall capacitance of a full cell should not exceed a quarter of that from a single electrode).

Fig. S4 shows the Ragone plot for the α-Fe_2O_3 NTs and α-Fe_2O_3 NTs-rGO composite in the potential window of 0 to -1 V in 1 M Na_2SO_4 aqueous electrolyte. Due to the high specific capacitance and wide working potential range, the α-Fe_2O_3 NTs- rGO composite provided a much higher energy and power density than the α-Fe_2O_3 NTs.

Supplementary discussion: Electrochemical capacitance performance of various iron oxides and iron oxide based composite materials in aqueous electrolyte compared with present study

In order to further evaluate the performance of this hybrid composite in a broader view, Table S3 summarizes the reported electrochemical capacitance performances of various iron oxide and iron oxide-based composite materials in aqueous electrolyte. As far as the electrolytes are concerned, in comparison with organic electrolytes, aqueous electrolyte used in ECs have the advantages of high ionic conductivity, low cost, non-flammability, good safety, and convenient assembly in air. Prior studies on the electrochemical capacitance of various iron oxide or hydroxide based electrodes in aqueous electrolytes have reported the specific capacitances ranging from 5 to 150 F/g. A few exceptions were reported by Wu *et al.* [23] and Zhitomirsky *et al.*[27] Zhitomirsky *et al.* achieved high specific capacitance of 210 F/g for porous γ-Fe_2O_3 in $Na_2S_2O_3$ electrolyte, under very strict conditions: at very low weight loading of 0.1 mg/cm^2. Wu *et al.* [23] achieved a specific capacitance of 170 F/g for electroplated Fe_3O_4 granules in Na_2SO_3 electrolyte. However, sulfite based aqueous electrolyte is not ideal for asymmetric ECs due to interference from the electrochemical oxidation of the sulfite anion, which will limit the available potential window at the positive electrode of an asymmetric EC (see supporting information in Ref. 34). Moreover, iron oxide-based ECs commonly suffered from cycling stability due to the reductive dissolution of the iron oxides when cycled to progressively negative potentials, especially when weak acidic Li_2SO_4 electrolyte was used.[28-30, 34] Long *et al.* proposed the use of borate-buffered Li_2SO_4 to reduce this problem.[34]

To further optimize the capacitance, cycling stability, and high rate property of iron oxide compounds, it is a current research trend to fabricate composites of iron oxides with electroactive and conducting materials (e.g. conducting polymers and carbon nanomaterials). Zhao *et al.*[26] demonstrated that by treating Fe_3O_4 nanowires with pyrrole, the specific capacitance in 0.1 M Na_2SO_3 electrolyte can be improved by 84 % from 106 F/g to 190 F/g, as well as better capacitance retention upon 500 cycles (from 75 % to 84 %). In addition, PANI-Fe_3O_4 in 1 M H_2SO_4 electrolyte was able to exhibit high

specific capacitance of 213 F/g and 146 F/g at current density of 1 mA/cm^2 and 5 mA/cm^2. However, the capacitance was found to reduce to to 85 % after 300 cycles, probably due to the unfavorable strong acidic electrolyte. Most recently, Yan *et al.*[13] reported a markedly high specific capacitance of 890 F/g and 480 F/g at current density of 1 A/g and 5 A/g, respectively, for the spray deposited Fe_3O_4-rGO composite. However, all the above examples used both corrosive KOH and H_2SO_4 which are not compatible for MnO_2-based positive electrodes or Na_2SO_3 with limited positive potential window. Herein, our α-Fe_2O_3 nanotubes-rGO composite electrodes in neutral electrolyte with high specific capacitance (181 F/g), high energy (90.8 Wh/kg) and high power density (1500 W/kg) at current density of 3 A/g, remarkably long cycle life, become a competitive alternative for their ultimate use as negative electrodes in aqueous asymmetric ECs. Besides, neutral electrolytes Na_2SO_4 used in our study, possesses additional advantages of environmental friendliness and convenience for end-user disposal than ECs based on strong acidic or alkaline electrolytes

Table S3. Electrochemical capacitance performance of various iron oxides and iron oxide based composite materials in aqueous electrolytes.

Iron oxides	Electrolyte	V range (V vs. Ag/AgCl)	C_m (F/g)	Method	Cycle life	Ref.
Fe_3O_4 electrocoagulated powder	1 M Na_2SO_4	-0.75 to 0.50	5.3	GS 15 mA/g	--	18
Fe_3O_4 electrocoagulated powder	1 M Na_2SO_3 1 M Na_2SO_4 1 M KOH	0 to 1.2	27.0 5.7 5.3	GS 15 mA/g	2000 (78 %)	19
Fe_3O_4 precipitated powder	0.1 M Na_2SO_4	-0.80 to 0.25	75	CV 10 mV/s	--	20, 21
Fe_3O_4 electrodeposited porous film	1 M Na_2SO_4	-0.60 to 0	105	CV 20 mV/s	--	22
Fe_3O_4 electroplated granules	1 M Na_2SO_3 1 M Na_2SO_4 1 M KOH	-0.70 to -0.20	170 25 3	CV 2 mV/s	--	23
Fe_3O_4 nanoparticles	1 M Na_2SO_4	-0.08 to 0.92	82	CV 50 mV/s	1000 (~60 %)	24
Fe_3O_4 octadecahedrons	1 M Na_2SO_3	-1.28 to 0.12	118	GS 6 mA	500 (~89 %)	25
Fe_3O_4 nanoparticles Fe_3O_4 nanowires Pyrrole treated-Fe_3O_4 nanowires	0.1 M Na_2SO_3	-1.28 to -0.08	12 106 190	GS 0.1 mA/cm^2	-- 500 (~75%) 500 (~84%)	26
γ-Fe_2O_3 porous film	0.25 M Na_2SO_4 0.25 M $Na_2S_2O_3$ 0.25 M $Na_2S_2O_3$	-0.98 to -0.18	43 82 210	CV 100 mV/s CV 2 mV/s	100 (~68 %)	27
α-Fe_2O_3 electrodeposited nanosheets	1 M Li_2SO_4	-0.98 to -0.18	135	CV 10 mV/s	500 (~70 %)	28, 29
α-Fe_2O_3 mesoporous nanostructures	1 M Li_2SO_4	-0.68 to -0.08	116	GS 0.75 A/g	1000 (~74 %)	30
β-FeOOH nanocolumns	1 M Li_2SO_4	-0.93 to -0.18	116	GS 0.5 A/g	--	31
α-LiFeO2 nanoparticles	0.5 M Li_2SO_4	-0.78 to -0.08	50	CV 10 mV/s	500 (~100 %)	32
PANI-Fe_3O_4 composites	1 M H_2SO_4	-0.08 to 0.67	213	GS 1 mA/cm^2	300 (~85 %)	33
FeOOH-coated carbon nanofoams	2.5 M Li_2SO_4 Buffered 2.5 M Li_2SO_4	-0.80 to 0.20	84 72	CV 5 mV/s	200 (~58 %) 1000 (~81%)	34
Fe_3O_4 nanoparticles rGO Fe_3O_4-rGO Fe_3O_4-rGO	1 M KOH	-0.88 to 0.12	104 139 480 890	GS 5 A/g GS 5 A/g GS 5 A/g GS 1 A/g	10000 (~100 %)	13
α-Fe_2O_3 nanotubes α-Fe_2O_3 NTs-rGO	1 M Na_2SO_4	-1.00 to 0	30 216	CV 2.5 mV/s	2000 (~92%) 2000 (~100%)	this study

References

1. H-M. Fan, J-B. Yi, Y. Yang, K-W. Kho, H-R. Tan, Z-X. Shen, J. Ding, X-W. Sun, M. C. Olivo, Y-P. Feng Single-crystalline MFe_2O_4 nanotubes/nanorings synthesized by thermal transformation process for biological applications. *ACS Nano* **2009**, 3, 2798-2808.
2. Wan, C.; Azumi, K.; Konno, H. Hydrated Mn (IV) oxide-exfoliated graphite composites for electrochemical capacitor. *Electrochim. Acta* **2007**, *52*, 3061-3066.
3. Wan, C.; Azumi, K.; Konno, H. Effect of synthesis route on the performance of hydrated Mn(IV) oxide-exfoliated graphite composites for electrochemical capacitors. *J. Appl. Electrochem.***2007**, *37*, 1055-1061.
4. Yan, J.; Fan, Z.; Wei, T.; Qie, Z.; Wang, S.; Zhang, M. Preparation and electrochemical characteristics of manganese dioxide/graphite nanoplatelet composites. *Mater. Sci. Eng. B* **2008**, *151*, 174-178.
5. Zhang, Y.; Li, H.; Pan, L., Lu, T.; Sun, Z. Capacitive behavior of graphene-ZnO composite film for supercapacitors. *J. Electroanal. Chem.* **2009**, 634, 68-71.
6. Li, F.; Song, J.; Yang, H.; Gan, S; Zhang, Q., Han, D.; Ivaska, A.; Niu, L. One-step synthesis of graphene/SnO_2 nanocomposites and its application in electrochemical supercapacitors. *Nanotechnol.* **2009**, 20, 455602-455607.
7. Chen, S.; Zhu, J.; Wu, X.; Han, Q.; Wang, X. Graphene oxide-MnO_2 nanocomposites for supercapacitor. *ACS Nano* **2010**, 4, 2822-2830.
8. Wang, H.; Casalongue, H. S..; Liang, Y.; Dai, H. $Ni(OH)_2$ nanoplates on graphene as advanced electrochemical pseudocapacitor materials. *J. Am. Chem. Soc.* **2010**, 132, 7472-7477.
9. Wang, B.; Park, J.; Wang, C.; Ahn, H.; Wang, G. Mn_3O_4 nanoparticles embedded into graphene nanosheets: preparation, characterization, and electrochemical properties for supercapacitors. *Electrochim. Acta.* **2010**, 55, 6812-6817.
10. Yan, J.; Fan, Z.; Wei, T.; Qian, W.; Zhang, M.; Wei, F. Fast and reversible surface redox reaction of graphene-MnO_2 composites as supercapacitor electrodes. *Carbon* **2010**, 48, 3825-3833.
11. Yan, J.; Wei, T.; Qian, W.; Shao, B.; Zhao, Q.; Zhang, L.; Fan, Z. Rapid microwave-assisted synthesis of graphene nanosheet/Co_3O_4 composite for supercapacitors. *Electrochim. Acta.* **2010**, 55, 6812-6817.
12. Chen, S.; Zhu, J.; Wang, X. One-step synthesis of graphene-cobalt hydroxide nanocomposites and their electrochemical properties. *J. Phys. Chem. C* **2010**, 114, 11829-11834.
13. Shi, W. H.; Zhu, J.; Sim, D. H.; Tay, Y. Y.; Lu, Z.; Zhang, X.; Sharma, Y.; Srinivasan, M.; Zhang, H.; Hng, H. H.; Yan, Q.; Achieving high specific capacitances in Fe_3O_4/reduced graphene oxide nanocomposites. *J. Mater. Chem.* **2011**, 21, 3422-3427.
14. Chen, Y.-L; Hu, Z.-A.; Chang, Y.-Q.; Wang, H.-W.; Zhang, Z.-Y.; Yang, Y.-Y.; Wu, H.-Y. Zinc oxide/reduced graphene oxide composites and electrochemical capacitance enhanced by homogeneous incorporation of reduced graphene oxide sheets in zinc oxide matrix. *J. Phys. Chem. C* **2011**, 115, 2563-2571.
15. Wang, L.; Wang, D.; Dong, X. Y.; Zhang, Z. J.; Pei, X. F.; Chen, X. J.; Chen, B.; Jin, J. Layered assembly of graphene oxide and Co-Al layered double hydroxide nanosheets as electrode materials for supercapacitors. *Chem. Commun.* **2011**, 47, 3556-3558.
16. Lee, J. W.; Ahn, T.; Soundararajan, D.; Ko, J. M.; Kim, J.-D. Non-aqueous approach to the preparation of reduced grapheme oxide/α-$Ni(OH)_2$ hybrid composites and their high capacitance behavior. *Chem. Commun.* **2011**, 47, 6305-6307.
17. Wang, Y.; Guo, C. X.; Liu, J.; Chen, T.; Yang, H.; Li, C. M. CeO_2 nanoparticles/grapheme nanocomposite-based high performance supercapacitor. *Dalton Trans.* **2011**, 40, 6388-6391.
18. Wu, N.-L.; Wang, S.-Y.; Han, C.-Y.; Wu, D.-S.; Shiue, L.-R. Electrochemical capacitor of magnetitie in aqueous electrolytes. *J. Power Sources* **2003**, *113*, 173-178.

19. Wang, S.-Y.; Wu, N.-L. Operating characteristics of aqueous magnetite electrochemical capacitors. *J. Appl. Electrochem.* **2003**, *33*, 345-348.
20. Brousse, T; Bélanger, D. A hybrid Fe_3O_4-MnO_2 capacitor in mild aqueous electrolyte. *Electrochem. Solid-State Lett.* **2003**, *6*, A244-A248.
21. Cottineau, T.; Toupin, M.; Delahaye, T.; Brousse, T.; Belanger, D. Nanostructured transition metal oxides for aqueous hybrid electrochemical supercapacitors. *Appl. Phys. A* **2006**, *82*, 599-606.
22. Chung, K.W.; Kim, K.B.; Han, S.-H.; Lee, H. Novel synthesis and electrochemical characterization of nano-sized cellular Fe_3O_4 thin film. *Electrochem. Solid-State Lett.* **2005**, *8*, A259-A262.
23. Wang, S.-Y.; Ho, K.-C.; Kuo, S.-L.; Wu, N.-L. Investigation of capacitance mechanisms of Fe_3O_4 electrochemical capacitors. *J. Electrochem. Soc.* **2006**, *153*, A75-A80.
24. Pang, S. P.; Khoh, W. H.; Chin, S. F. Nanoparticulate magnetite thin films as electrode materials for the fabrication of electrochemical capacitors. *J. Mater. Sci.* **2010**, *45*, 5598-5604.
25. Chen, J.; Huang, K.; Liu, S. Hydrothermal preparation of octahedron Fe_3O_4 thin film for use in an electrochemical supercapacitor. *Electrochim. Acta* **2009**, *55*, 1-5.
26. Zhao, X.; Johnson, C.; Crossley, A.; Grant, P. S. Printable magnetite and pyrrole treated magnetite based electrode for supercapacitors. *J. Mater. Chem.* **2010**, *20*, 7637-7644.
27. Nagarajan, N.; Zhitomirsky, I. Cathodic electrosynthesis of iron oxide films for electrochemical supercapacitors. *J. App. Electrochem.* **2006**, *36*, 1399-1405.
28. Wu, M.-S.; Lee, R.-H.; Jow, J.-J.; Yang, W.-D.; Hsieh, C.-Y.; Weng, B.-J. Nanostructured iron oxide films prepared by electrochemical methods for electrochemical capacitors. *Electrochem. Solid-State Lett.* **2009**, *12*, A1-A4.
29. Wu, M.-S.; Lee, R.-H. Electrochemical growth of iron oxide thin films with nanorods and nanosheets for capacitors. *J. Electrochem. Soc.* **2009**, *156*, A737-A743.
30. Wang, D.; Wang, Q.; Wang, T. Controlled synthesis of mesoporous hematite nanostructures and their application as electrochemical capacitor electrodes. *Nanotechnology* **2011**, *22*, 135604-135615.
31. Jin, W-H.; Cao, G-T.; Sun, J-Y. Hybrid supercapacitor based on MnO_2 and columned FeOOH using Li_2SO_4 electrolyte solution. *J. Power Sources* **2008**, 175, 686-691.
32. Santos-Pena, J.; Crosnier, O.; Brousse, T. Nanosized α-$LiFeO_2$ as electrochemical supercapacitor electrode in neutral sulfate electrolytes. *Electrochim. Acta* **2010**, 55, 7511-7515.
33. Radhakrishnan, S.; Prakash, S.; Rao, C. R. K.; Vijayan, M. Organically soluble bifunctional polyaniline-magnetite composites for sensing and supercapacitor applications. *Electrochem. Solid State Lett.* **2009**, 12, A84-A87.
34. Sassin, M. B.; Mansour, A. N.; Pettigrew, K. A.; Rolison, D. R.; Long, J. L. Electroless deposition of conformal nanoscale iron oxide on carbon nanoarchitectures for electrochemical charge storage. *ACS Nano* **2010**, 4, 4505–4514.